Electronic Supplementary Information for

Advancing towards ready-to-use solid oxide fuel cells: 5-minute cold start-up with high power performance

Hyeseong Jeong,[ab] Channyung Lee,[c] Ji-Won Son,[ad] Seung Yong Lee,[e] Kyung Joong Yoon,[a] Dongwook Shin,[b] Mansoo Choi,[c] Sung Soo Shin,*[af] and Hyoungchul Kim*[a]

[a]*Energy Materials Research Center, Korea Institute of Science and Technology, Seoul 02792, Republic of Korea*

[b]*Division of Materials Science and Engineering, Hanyang University, Seoul 04763, Republic of Korea.*

[c]*Department of Mechanical and Aerospace Engineering, Seoul National University, Seoul 08826, Republic of Korea.*

[d]*Graduate School of Energy and Environment (KU-KIST Green School), Korea University, Seoul 02841, Republic of Korea.*

[e]*Materials Architecturing Research Center, Korea Institute of Science and Technology, Seoul 02792, Republic of Korea.*

[f]*Department of Mechanical System Engineering, Kumoh National Institute of Technology, Gyeongbuk 39177, Republic of Korea.*

***Corresponding authors**

ssshin@kumoh.ac.kr (S.S. Shin), hyoungchul@kist.re.kr (H. Kim)

Materials and Methods

Fabrication of thin-film solid oxide fuel cells (SOFCs)

Tape casting and high-temperature lamination processes were used to fabricate an anode substrate. The slurry used for tape casting to prepare a porous anode-supporting layer (ASL) consisted of a 46:49:5 weight ratio of $Ce_{0.9}Gd_{0.1}O_{1.95}$ (CGO; Rhodia), NiO (Mechema), and polymethyl methacrylate (Sunjin Chemical). Ethyl alcohol and toluene were used as solvents. KD-1 (Sigma Aldrich), dibutyl phthalate (Sigma Aldrich), and polyvinyl butyral (Sigma Aldrich) were used as dispersants, plasticizers, and binders, respectively. A slurry for the anode-functional layer (AFL) without a pore former was composed of CGO:NiO at a 49:51 weight ratio. The anode substrate was laminated by pressing 2 MPa at 80 °C on several stacked sheets of ASL and one sheet of AFL to a final thickness of 1 mm. The pressed body was subsequently sintered in a furnace at 1350 °C for 4 h. To prepare a button cell, the sintered anode substrate was cut into 2 cm × 2 cm pieces. Radio frequency (RF) magnetron sputtering and pulsed laser disposition (PLD) processes were then used to deposit the electrolyte and cathode layers, respectively. To produce a nanoscale AFL (nAFL), NiO-CGO composed of CGO:NiO at a 49:51 weight ratio was deposited on the AFL by sputtering at 700 °C for 9 h (100 W RF power at a working pressure of 5 mTorr) in an Ar atmosphere, followed by heat treatment at 1200 °C for 1 h. An electrolyte multilayer consisting of layers of CGO, Y_2O_3-stabilized-ZrO_2 (YSZ), and CGO was then deposited on the nAFL by sputtering for 6, 1, and 2 h, respectively. A $La_{0.6}Sr_{0.4}CoO_{3-\delta}$ (LSC; Kceracell) cathode layer was deposited on the CGO by PLD at 700 °C for 2 h (120 mJ KrF laser with a working pressure of 300 mTorr) in an O_2 atmosphere. As the final step, electrochemical activation of the anodic structure using a pre-reduction process was carried out for ready-to-use purpose. The NiO-CGO anode was transformed to Ni-CGO by reducing it for 8 h in a 3% humidified H_2 atmosphere at 600 °C. Thus, immediate power delivery was possible as soon as the desired temperature was reached, without any further reduction step during cell operations.

Packaging assembly for rapid start-up operations

To construct a unit cell assembly used for the ready-to-use SOFC (RTU-SOFC) system, we used several components, as shown in Figure 1a. Cu-Mn/Au mesh and Ni foam were used as current collectors for the cathode and anode, respectively. A mica sealant was used as the sealing gasket, and metal nuts and bolts were used to fasten the upper and lower endplates. In addition, to prevent short-circuiting between two plates, a metal bolt was wrapped with an insulating tube. An Inconel disc spring (Inconel X-750, SJ Korea) was placed at each corner of the lower endplate to maintain uniform pressure in all parts of the cell. Finally, the stand-alone unit-cell assembly was fastened with a torque force of 20 kgf-cm. Furthermore, 12 tungsten halogen lamps (providing a total of 18 kW) were used as an infrared heat source. The temperature profiles were measured using K-type thermocouples at two points, namely, the centre of the unit-cell assembly and the heater module. The unit-cell assembly loaded in the centre of the quartz was heated according to the optimized temperature setting profile (T_{set}) and reached the target temperature (T_{target}, 600 or 500 °C) within 5 min. To reach a T_{target} of 500 °C, the system temperature was elevated to 700 °C for 60 s, maintained at 700 °C for 140 s, cooled to 513 °C for 40 s, and subsequently maintained at 620 °C. To reach a T_{target} of 600 °C, the system temperature was elevated to 715 °C for 60 s, maintained at 715 °C for 190 s, cooled to 620 °C for 40 s, and then maintained at 620 °C. Under the T_{set} conditions, the temperature of the unit-cell assembly (T_{cell}) converged to 600 or 500 °C within 5 min after commencing the operation.

Characterization of the RTU-SOFC system

During the evaluation of electrochemical cell performance and thermal cycling tests, air and 3% humidified H_2 were continuously supplied at gas flows of 200 and 200 sccm, respectively. However, the thermal cycling experiments at 500 °C were conducted by shutting off the hydrogen supply in the “Power-Off mode”. This hydrogen shutoff was performed by setting the flow meter to zero and closing the valve. The potential-current density curve and impedance data were obtained using an electrochemical analyzer (Iviumstat, Ivium Technologies). To observe the microstructure of the cell, we used scanning electron microscopy (SEM; Regulus 8230, Hitachi), a focused-ion beam (Helios 5 HX FIB, Thermo Scientific) imaging modalities, transmission electron microscopy

(TEM; Talos F200X, FEI), and energy dispersive X-ray spectroscopy (EDS; SuperX EDS system, Bruker).

Electrical characterization of the Cu-Mn foam

To measure the area-specific resistance (ASR) of the Cu-Mn foam, we cut the foam into a 1×1 cm^2 size pieces and performed assembly by stacking on jig. Mica sealant was inserted between the plates and fastened with bolts wrapped with insulation tubes to prevent short circuiting. To measure the electrical properties of the foam, an operation setting of T_{target} at 500 °C was used. The impedance was measured in the frequency range of 1 to 10,000 Hz at 30-s intervals for the initial 5 min after heating, and then at 60, 120, 180 min, respectively.

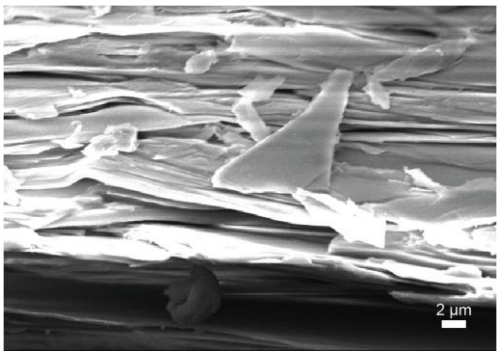

Fig. S1 A cross-section SEM image of mica sealant.

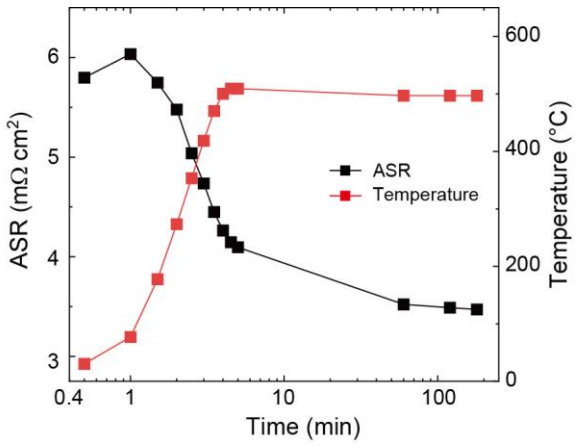

Fig. S2 Variations in ASR of Cu-Mn foam and the measured temperature as a function of operation time.

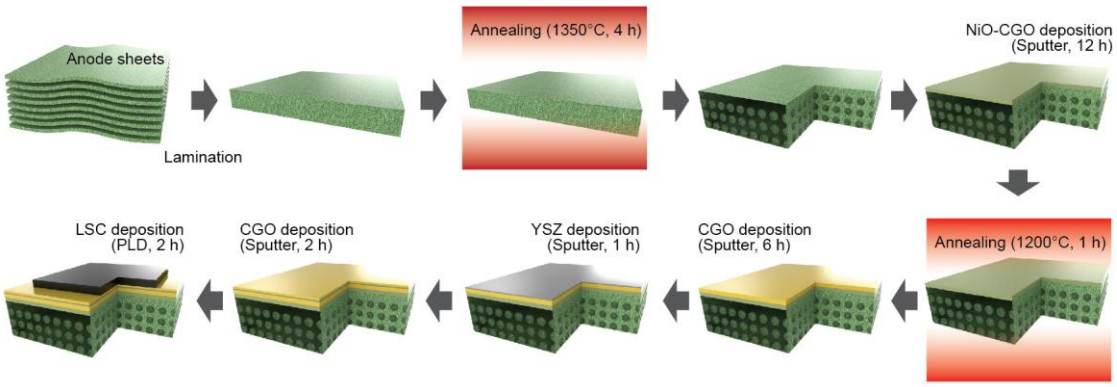

Fig. S3 Schematic illustrations of the fabrication process for a thin-film-based SOFC.

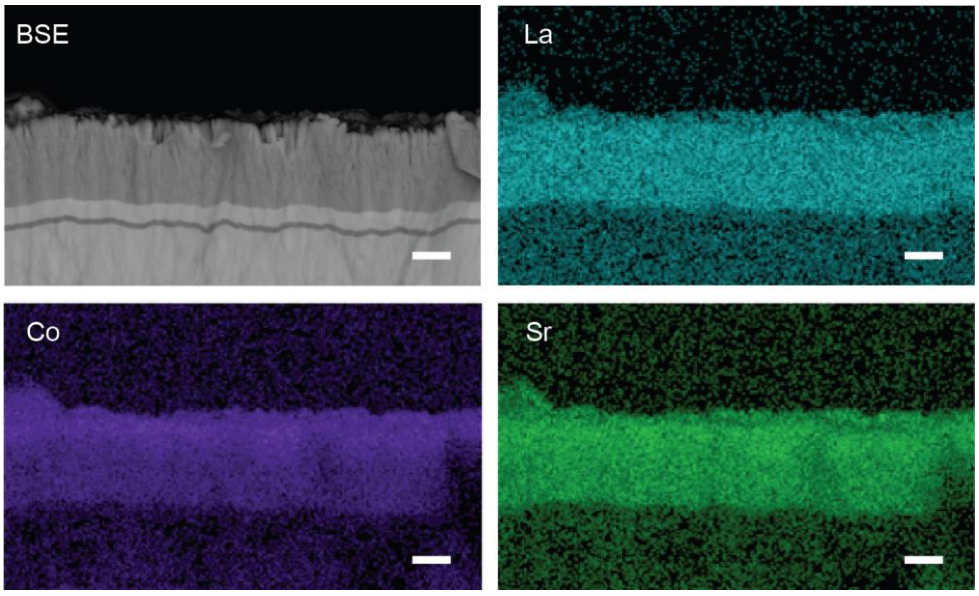

Fig. S4 Cross-section view BSE image of thin-film-based SOFC and corresponding EDS results. All scale bars correspond to 2 μm.

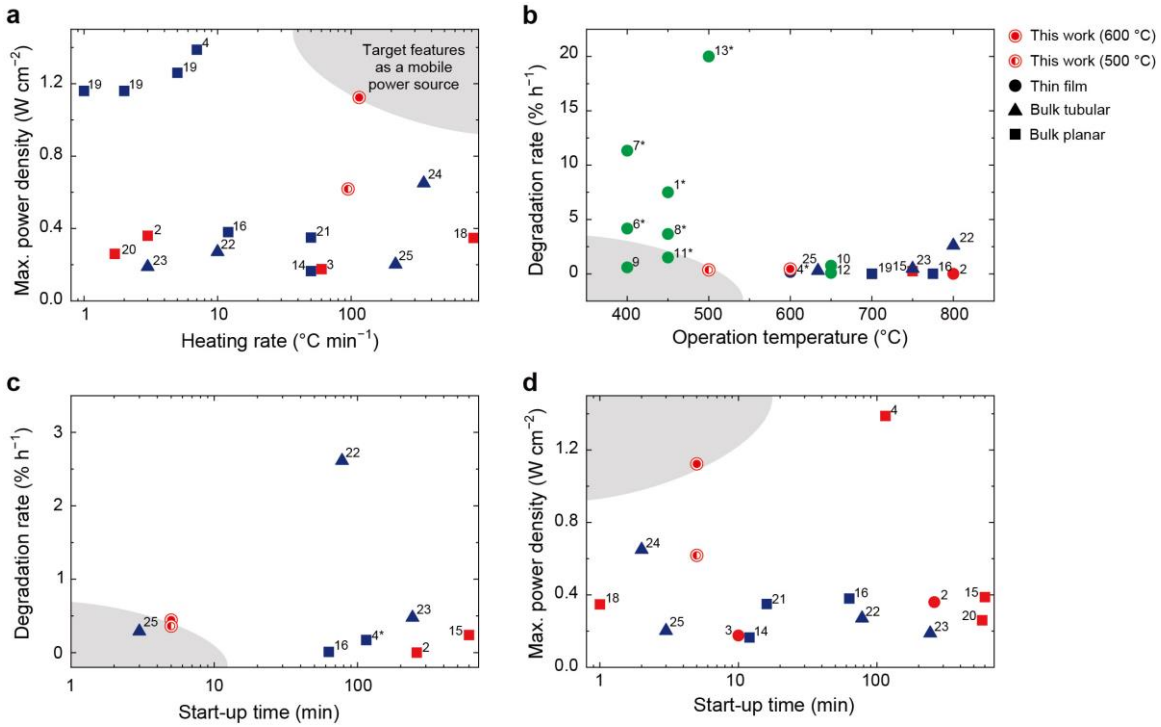

Fig. S5 Comparison of the heating rate in this work with that of previously reported SOFCs based on rapid thermal cycling tests. Red and blue color symbols indicate thermal cycling experiments of cold (from room temperature to T_{target}) and warm (from elevated temperature to T_{target}) start-up, respectively. The green symbols are tests that do not accurately describe the start temperature of the thermal cycling. The degradation rates are mainly calculated from potential (or current) changes, except for a few cases ('*' symbols) obtained from power changes. The characteristics of the SOFCs we aim for as a mobile power source are shown in the gray area (low degradation rate, rapid thermal cycling, and high power density). Detailed information and results are listed in Table S1.

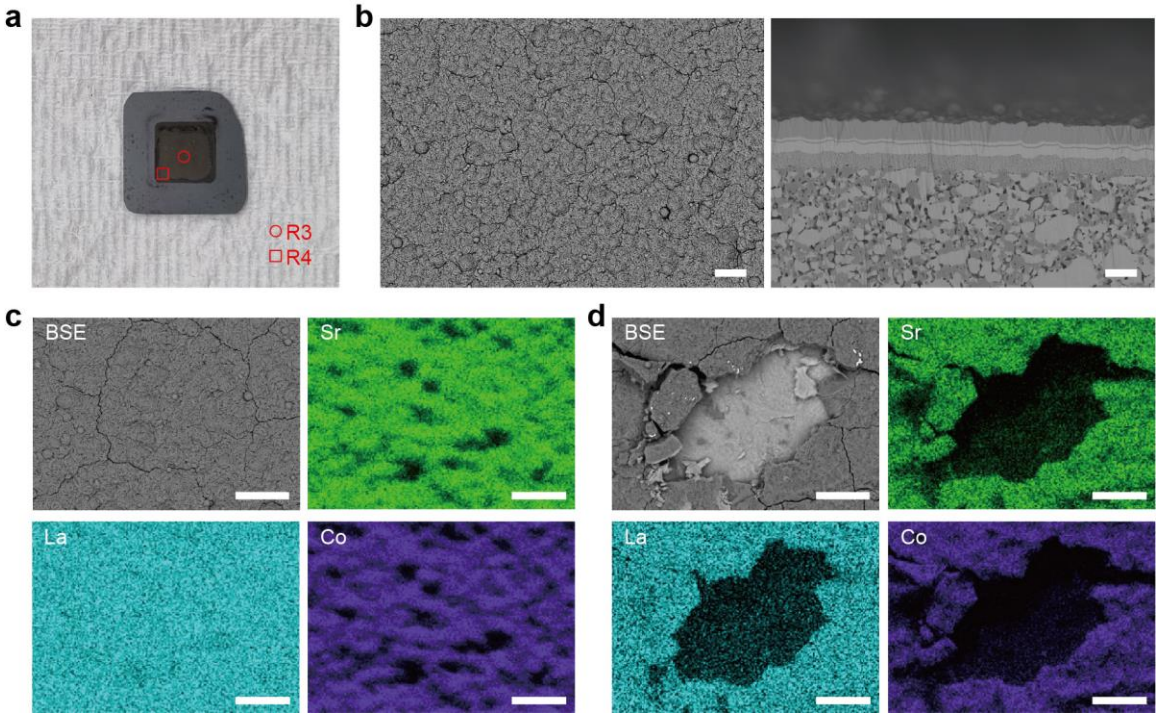

Fig. S6 (a) A photograph and (b) SEM-BSE images (left: top-view, right: cross-sectional view) of a cell after 15 cycles of operation at 500 °C. SEM-BSE images and EDS for Sr, La, and Co in the upper surface of the (c) R3 and R4 regions. All scale bars correspond to 5 μm.

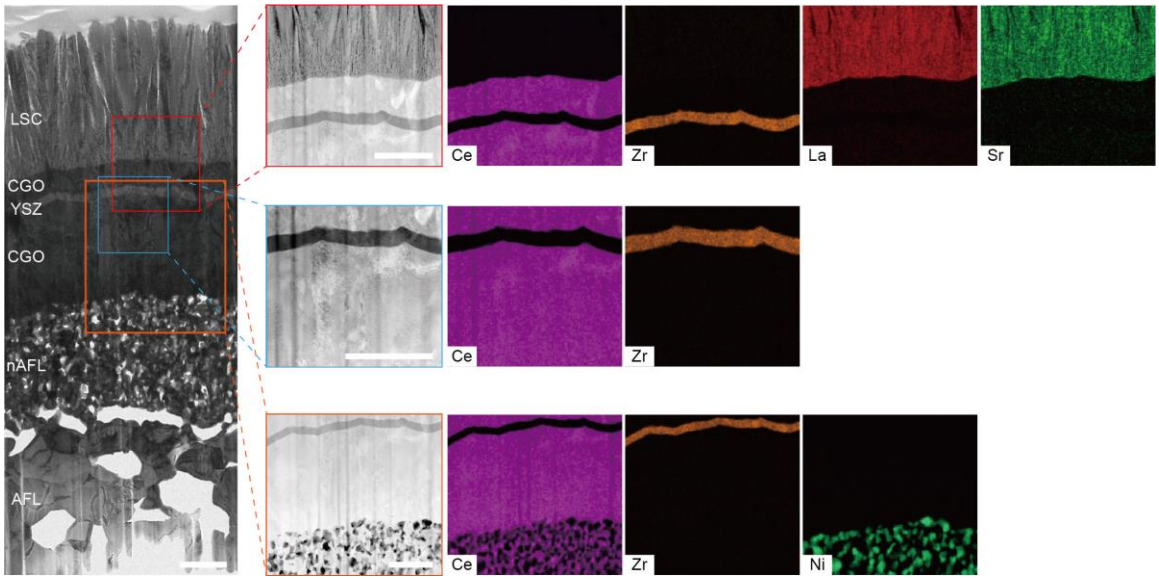

Fig. S7 TEM-EDS images of a cell after 15 cycles of operation at 600 °C. Cross-sectional TEM images of whole cell (left) and magnified region and EDS for Ce, Zr, La, Sr, and Ni at cathode/electrolyte (top), electrolyte (middle), and electrolyte/anode (bottom). All scale bars correspond to 2 μm.

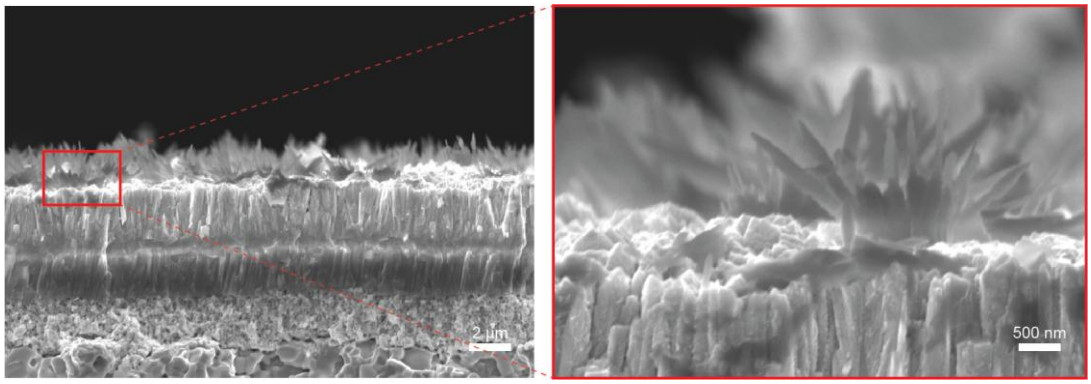

Fig. S8 Magnified SEM images of needle-shaped microstructures after the thermocycling test.

Table. S1 A comparison of the electrochemical performance and operating information of the system developed this study with those of previously reported SOFCs based on rapid thermal cycling tests.

Cell type	Heating type	Heating rate (°C min^{-1})	Start-up time (min)	Maximum power density (W cm^{-2})	Voltage degradation rate (% h^{-1})	Power degradation rate (% h^{-1})	Operation Temperature (°C)	Temperature range (°C)	Number of cycles	Ref.
Thin film	Lamp heater	115	5	1.123	0.442	2.288	600	25–600	15	This work
Thin film	Lamp heater	95	5	0.618	0.36	1.722	500	25–500	15	This work
Thin film	Lamp heater	N/A	N/A	0.035	N/A	7.5	450	N/A	N/A	1
Thin film	Furnace	3	259	~0.36	0.0004	0.013	800	23–800	13	2
Thin film	Furnace	60	10	0.176	N/A	N/A	600	25–600	12	3
Thin film	Furnace	7	115	1.388	N/A	0.172	600	400–600	50	4
Thin film	N/A	N/A	N/A	0.24	N/A	N/A	400	25–700	3	5
Thin film	N/A	N/A	N/A	0.53	N/A	N/A	400	25–700	3	5
Thin film	N/A	N/A	N/A	1.037	N/A	4.167	400	N/A	N/A	6
Thin film	N/A	N/A	N/A	1.3	N/A	11.333	400	N/A	N/A	7
Thin film	N/A	N/A	N/A	0.18	N/A	3.667	450	N/A	N/A	8
Thin film	N/A	N/A	N/A	0.062	0.588	N/A	400	N/A	N/A	9
Thin film	N/A	N/A	N/A	3.37	0.75	N/A	650	N/A	N/A	10
Thin film	N/A	N/A	N/A	0.004	N/A	1.5	450	N/A	N/A	11
Thin film	N/A	N/A	N/A	1.735	0.08	N/A	650	N/A	N/A	12
Thin film	N/A	N/A	N/A	1.34	N/A	20	500	N/A	N/A	13
Bulk	Furnace	50	12	0.165	N/A	N/A	600	170–600	100	14
Bulk	Furnace	N/A	~600	~0.388	0.24	~0.66	750	25–750	15	15
Bulk	Furnace	12	63	~0.38	0.01	0.01	775	100–775	13	16
Bulk	Heating stage	9	92	N/A	N/A	N/A	N/A	20–850	3	17
Bulk	Flame	825	1	0.348	N/A	N/A	850	25–850	5	18
Bulk	N/A	1	N/A	1.16	0.009	0.016	700	400–700	45	19
Bulk	N/A	2	N/A	1.16	0.008	0.016	700	400–700	57	19
Bulk	N/A	5	N/A	1.26	0.019	0.062	700	400–700	118	19
Bulk	N/A	1.7	574	0.26	N/A	N/A	1000	25–1000	12	20
Bulk	N/A	50	16	0.35	N/A	N/A	900	200–800	50	21
Tubular	N/A	10	78	0.271	2.613	N/A	800	650–800	14	22
Tubular	Furnace	3	242	0.188	0.477	0.564	750	200–750	100	23
Tubular	Furnace	350	2	~0.65	N/A	N/A	700	100–700	5	24
Tubular	Flame	215	3	0.202	0.29	N/A	634	200–634	200	25

References

1. S. Ji, I. Chang, Y. H. Lee, J. Park, J. Y. Paek, M. H. Lee and S. W. Cha, *Nanoscale Res. Lett.*, 2013, **8**, 48.
2. J. V. herle, D. Perednis, K. Nakamura, S. Diethelm, M. Zahid, A. Aslanides, T. Somekawa, Y. Baba, K. Horiuchi, Y. Matsuzaki, M. Yochimoto and O. Bucheli, *J. Power Sources*, 2008, **182**, 389–399.
3. Z. Wang, J. O. Berghaus, S. Yick, C. Deces-Petit, W. Qu, R. Hui, R. Maric and D. Ghosh, *J. Power Sources*, 2008, **176**, 90–95.
4. H.-S. Noh, K. J. Yoon, B.-K. Kim, H.-J. Je, H.-W. Lee, J.-H. Lee and J.-W. Son, *J. Power Sources*, 2014, **249**, 125–130.
5. Y.-W. Ju, T. Inagaki, S. Ida and T. Ishihara, *J. Electrochem. Soc*, 2011, **158**, B825–B830.
6. K. Kerman, B.-K. Lai and S. Ramanathan, *J. Power Sources*, 2011, **196**, 2608–2614.
7. J. An, Y.-B. Kim, J. Park, T. M. Gur and F. B. Prinz, *Nano Lett.*, 2013, **13**, 4551–4555.
8. S. Ha, P.-C. Su and S.-W. Cha, *J. Mater. Chem. A*, 2013, **1**, 9645.
9. C.-W. Kwon, J.-I. Lee, K.-B. Kim, H.-W. Lee, J.-H. Lee and J.-W. Son, *J. Power Sources*, 2012, **210**, 178–183.
10. H. Ren, Y. H. Lee, E. A. Wu, H. Chung, Y. S. Meng, E. E. Fullerton and N. Q. Minh, *ACS Appl. Energy Mater.*, 2020, **3**, 8135–8142.
11. J.-G. Yu, B. C. Yang, J. W. Shin, S. Lee, S. Oh, J. -H. Choi, J. Jeong, W. Noh and J. An, *Ceram. Int.*, 2019, **45**, 3811–3815.

12. J. H. Park, S. M. Han, B.-K. Kim, J.-H. Lee, K. J. Yoon, H. Kim, H.-I. Ji and J.-W. Son, *Electrochim. Acta.*, 2019, **296**, 1055–1063.

13. C.-C. Chao, C.-M. Hsu, Y. Cui and F. B. Prinz, *ACS Nano*, 2011, **5**, 5692–5696.

14. A. M. Dayaghi, K. J. Kim, S. J. Kim, S. Kim, H. Bae and G. M. Choi, *J. Power Sources*, 2017, **354**, 74–84.

15. J. Pan, J. Yang, D. Yan, J. Pu, B. Chi and J. Li, *Int. J. Hydrogen Energy*, 2020, **45**, 17927–17934.

16. A. Hagen, A. C. Wulff, P. Zielke, X. Sun, B. Talic, I. Ritucci, H. L. Frandsen, S. H. Jensen, W. R. Kiebach and P. V. Hendriksen, *Int. J. Hydrogen Energy*, 2020, **45**, 29201–29211.

17. T. Klemenso, C. C. Appel and M. Mogensen, *Electrochem. Solid-State Lett.*, 2006, **9**, A403–A407.

18. X. Zhu, B. Wei, Z. Lü, L. Yang, X. Huang, Y. Zhang and M. Liu, *Int. J. Hydrogen Energy*, 2012, **37**, 8621–8629.

19. J.-S. Shin, M. S. Jo, K. Park, K. M. Park, J. S. Ahn, H.-T. Lim and J.-Y. Park, *ACS Appl. Mater. Interfaces*, 2021, **13**, 49868–49878.

20. S. Taniguchi, M. Kadowaki, T. Yasuo, Y. Akiyama, Y. Miyake and K. Nishio, *J. Power Sources*, 2000, **90**, 163–169.

21. Y. B. Matus, L. C. D. Jonghe, C. P. Jacobson and S. J. Visco, *Solid State Ion.*, 2005, **176**, 443–449.

22. H. Lu, Z. Huang, G. Zhang, T. Chen and S. Wang, *Int. J. Hydrogen Energy*, 2022, **47**, 33420–33428.

23. W. Guan, Z. Du, J. Wang, L. Jiang, J. Yang and X. -D. Zhou, *Int. J. Hydrogen Energy*, 2020, **45**, 19840–19846.

24. M. C. Tucker, G. Y. Lau, C. P. Jacobson, L. C. DeJonghe and S. J. Visco, *J. Power Sources*, 2008, **175**, 447–451.

25. R. J. Milcarek, V. P. DeBiase and J. Ahn, *Energy*, 2020, **196**, 117148.